ADVANCED FUNCTIONAL MATERIALS
www.afm-journal.de

Uniting Ultrahigh Plasticity with Near-Theoretical Strength in Submicron-Scale Si via Surface Healing

Wei Xu, Jinhua Yu, Jun Ding, Yunna Guo, Lei Deng, Liqiang Zhang, Xiaoxuan Wan, Shaochuan Zheng, Yuecun Wang, and Zhiwei Shan**

As a typical hard but brittle material, Si tends to fracture abruptly at a stress well below its theoretical strength, even if the tested volume goes down to submicron scale, at which materials are usually nearly free of flaws or extended defects. Here, via the thermal–oxidation–mediated healing of the surface that is the preferred site for cracks or dislocations initiation, the premature fracture can be effectively inhibited and the over 50% homogeneous plastic strain with the near-theoretical strength (twice the value of the unhealed counterpart) are united in submicron-sized Si particles. In situ transmission electron microscope observations and atomistic simulations elucidate the confinement effect from the passivated and smoothened thermal oxide, which retards the dislocation nucleation and transforms the dominant deformation mechanism from partial dislocation to the more mobile full dislocation. This work demonstrates an effective and feasible surface engineering pathway to optimize the mechanical properties of Si at small scales.

1. Introduction

The ever increasingly versatile and important applications not only challenge the functional performances of silicon (Si) but also have a high demand for its structural and load-bearing reliability, which mainly depends on the deformability and strength of Si.[1] However, as a typically brittle material, Si is inclined to crack or fracture abruptly at the stress far below its theoretical strength,[2] causing catastrophic failure and impeding more extensive applications of Si.[3] Therefore, how to inhibit the premature fracture of Si and improve its mechanical reliability has been a subject of many studies in both fundamental and applied researches.

The room-temperature brittleness of Si originates from the strong-covalent-bonds-induced high lattice friction for dislocation slip and high sensitivity to preexisting flaws.[4] With the miniaturizing development of Si-based components, the number of internal flaws in the Czochralski-grown small-volume single-crystal Si has been very low. The correspondingly increased surface-to-volume ratio makes the surface blemishes (such as the tiny pit or ledge) become the dominant stress raisers, which act as the potential nucleation point of dislocations or cracks and cause the premature fracture failure of Si.[5] Recent years have seen continuous efforts in improving the surface quality of Si to eliminate these stress raisers. The surface roughness of Si wafer has been lowered down to sub-angstrom via chemical mechanical polishing.[6] A newly developed edge-blunting technique can effectively mitigate room-temperature brittleness by blunting the sharp corners in the marginal regions of Si wafers.[1a] This surface engineering plays a more significant role in improving the deformability of Si at micron or submicron scale (the characteristic size of Si structural components in many microdevices).[7] It has been reported that the high elastic strain limit (≈10%) as well as the near-theoretical strength can be achieved in micropillars fabricated by the high-resolution lithographic etching[8] or Si nanowires grown via the vapor-liquid-solid process,[9] owing to their smooth surface and defects-scarce single crystal structure. Though the premature fracture of Si (especially the submicron-sized or smaller Si with high-quality surface) can be inhibited, the intervening plastic deformation prior to the mechanical failure is usually quite small, showing no obvious indication before the abrupt fracture or shear-off, i.e., the brittleness remaining to be a potential threat.[3a,10] The room-temperature plasticity in Si could be triggered via the surface treatment as well. It has been found that the focused ion beam irradiation-induced surface amorphization can provide a good confinement effect on the pristine interior, inhibiting the crack initiation and promoting the dislocation or phase transformation-mediated plastic deformation in Si

W. Xu, X. Wan, S. Zheng, Y. Wang, Z. Shan
Center for Advancing Materials Performance from the Nanoscale (CAMP-Nano) & Hysitron Applied Research Center in China (HARCC)
State Key Laboratory for Mechanical Behavior of Materials
Xi'an Jiaotong University
Xi'an 710049, China
E-mail: yuecunwang@xjtu.edu.cn; zwshan@mail.xjtu.edu.cn

J. Yu, J. Ding
Center for Alloy Innovation and Design (CAID)
State Key Laboratory for Mechanical Behavior of Materials
Xi'an Jiaotong University
Xi'an 710049, China

Y. Guo, L. Deng, L. Zhang
Clean Nano Energy Center
State Key Laboratory of Metastable Materials Science and Technology
Yanshan University
Qinhuangdao 066004, China

The ORCID identification number(s) for the author(s) of this article can be found under https://doi.org/10.1002/adfm.202404694

DOI: 10.1002/adfm.202404694

micropillars.[11] But the surface damage caused by ion irradiation severely decreases the yield strength of Si micropillars, which is much lower than the theoretical strength.[12]

Here a question naturally arises, how to achieve the near-theoretical strength and the high plastic deformability in Si concurrently? To this end, first, we should resort to the single-crystal Si samples that are initially nearly free of dislocations or other extended defects, such that the chances for premature fracture before yielding are minimized. As mentioned above, a feasible way is to reduce the physical dimensions of the tested volume down to submicron scale. In addition to the pristine internal structure, a passivated (smooth and defectless) surface is necessary for suppressing the surface dislocation nucleation or crack initiation at low applied stresses.[13] However, the naturally-grown oxide layer on Si that forms during partial surface oxidization at ambient temperatures is not fully passivated. It has been reported that the native oxide may obviously decrease the strength of Si nanobeams, supposedly owing to the partial oxidation-induced surface stress raisers or defects.[14] Therefore, it is desirable, if the submicron-scale Si has a smooth and defectless surface coating, to reach a very high value (approaching the ideal strength). Furthermore, the passivated surface is expected to serve as an effective barrier to stop dislocations from escaping out of the free surface[15] and result in dislocation back stress, which would not only ameliorate the local stress in the vicinity of potential crack nucleation sites but also give rise to the strain hardening,[16] making the homogeneous plastic deformation without cracking or localized shear-off possible.

Here, we propose a thermal–oxidation–mediated surface healing, by which the stress raisers on Si can be incorporated in the fully-oxidized layer and the defects would be eliminated largely. Our in situ quantitative compression experiments inside a transmission electron microscope (TEM) demonstrate that ultrahigh plasticity with near-theoretical strength can be concurrently achieved in the thermally-oxidized Si spherical particles with several hundreds of nanometers in diameter. The choice of spherical single-crystal particles is made here mainly because the spherical geometry ensures that the maximum stress site is located in the interior rather than on the surface when it is loaded,[17] and it is ideally suited for experimentally achieving the near-theoretical strength. Since the possibility of surface dislocation nucleation and crack initiation could be effectively reduced or even eliminated. Besides, Si particles themselves have many outstanding properties and have been widely used in electronics, photonics, lithium-ion batteries, and biotechnology, of which the design and use highly depend on the mechanical reliability of Si particles.[18]

2. Results and Discussion

2.1. In situ Compression of the as-Grown Si Particles

Si spherical particles were synthesized using a thermal plasma deposition technique.[19] These particles are inevitably covered by a thin oxide layer upon exposure to air at ambient temperature. The naturally-grown oxide is 2–3 nm thick regardless of the particle size (see the bright-field TEM image and thickness distribution in the inset histogram in Figure S1, Supporting Information). Some as-grown Si particles with the diameter D ranging from 150–600 nm were in situ compressed, feasible using a nanomechanical testing system inside TEM. A typical example is displayed in **Figure 1**. Under TEM imaging, the interior of the selected Si particle (D = 257 nm) is primarily defects-scarce, and the concentric thickness fringes can be clearly seen in the interior. This individual particle was compressed by a flat diamond punch along the ≈<111> direction with the acquisition of the real-time deformation process and load-displacement data. Figure 1 shows the load versus normal compressive strain (defined as the compression displacement of the particle divided by D) curve with the inserted snapshots from Video S1 (Supporting Information). The Si particle initially undergoes elastic deformation (the apparent elastic strain of ≈8%), and then fractures into two pieces abruptly, corresponding to a very big strain burst in the compressive curve. The maximum contact stress of the particle, designated as the "compressive strength" that stands for the capacity of a particle to withstand loads without cracking, is about 7.8 GPa. Prior to the catastrophic splitting crack, dislocations slipping along {111} planes have been observed (the dashed lines show the projections of slipping traces and the cleavage planes). This indicates that plastic deformation is set in by the surface nucleation of dislocations, at a stress lower than 7.8 GPa. The surface stress raisers may serve as the predominant sites for the dislocation emission. The slipping of dislocations is localized on two or three intersecting glide planes and slip bands intersect at a point where dislocations pile up, causing an obvious stress concentration. The crack initiates and propagates quickly at the stress raisers, giving rise to the splitting of the particle. Though the moment of fracture has not been recorded clearly due to the very fast crack formation and propagation, a wedge that is formed by the intersecting slip bands and causes the following splitting of the particle can be clearly seen just before the cracking. From post-mortem characterizations of a fractured Si particle (Figure S2, Supporting Information), we can see that the dislocation-mediated plastic deformation mainly occurred near the contact areas, and other parts of the particle deformed elastically.

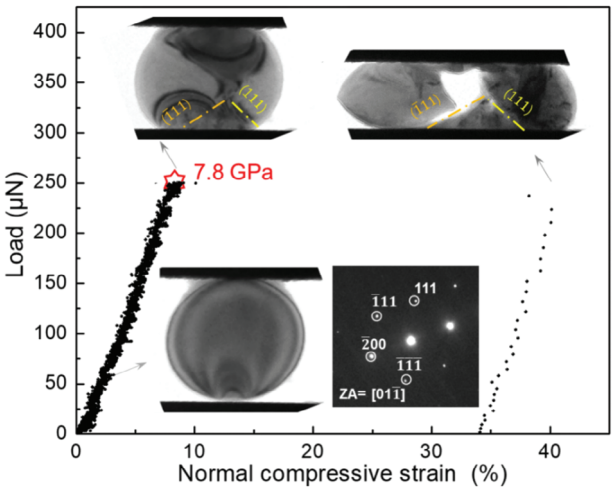

Figure 1. In situ compression of a typical as-grown Si particle (with the diameter D = 257 nm) inside TEM. The inset TEM images in the load versus normal compressive strain curve demonstrate the snapshots from the in situ TEM video recording the deformation and fracture process of the particle.

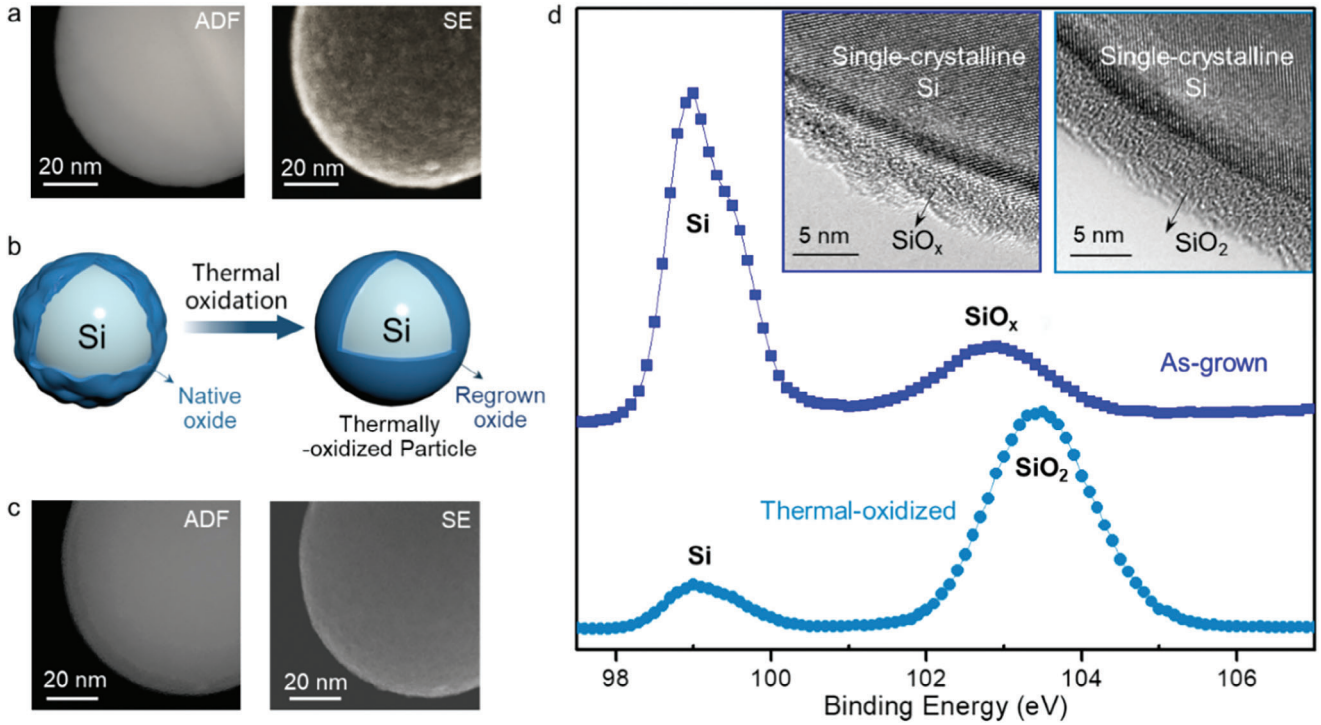

Figure 2. Characterizations of the as-grown and thermally-oxidized Si particles. a) A typical as-grown Si particle taken under annular-dark-field (ADF) STEM image and the corresponding secondary electron (SE) image. b) The schematic diagram shows the incorporation of the surface stress raisers and defects into the regrown oxide via thermal oxidation. c) A typical thermally-oxidized Si particle taken under annular-dark-field (ADF) STEM image and the corresponding secondary electron (SE) image. d) 2p Si XPS spectra of the as-grown and thermally-oxidized Si particles. The inset HRTEM images show the native (SiO_x) and thermal oxide (SiO_2) on Si particles.

2.2. Surface Passivation of Si Particles via the Well-Controllable Thermal Oxidation

As previously mentioned, the naturally-grown oxide layer comes from partial surface oxidization and is not fully passivated. Therefore, instead of protecting the internal Si structure from cracking, the surface stress raisers and defects in the native oxide may lower the strength of the particles greatly. To demonstrate the surface condition of as-grown Si particles, we further examined them using a Cs-corrected scanning-TEM (STEM, 200 kV) equipped with an atomic-resolution secondary electron (SE) detector that can obtain the information from the very top surface of materials and offer higher spatial resolution with more faithful surface information compared with the common scanning electron microscope (SEM). **Figure 2**a displays the Annular-dark-field (ADF) STEM image and the corresponding SE image of the same Si particle. Surprisingly, the surface that seems to be quite smooth under the STEM imaging, is actually rough and bumpy just like the "lunar surface" under the simultaneous SE imaging. To obtain a smoother and well-passivated surface, we propose to regrow a thin oxide layer on Si particles via heating them in an oxygen atmosphere (as illustrated in Figure 2b), during which Si atoms diffuse into the native oxide and react with incoming oxidants.[20] Surface defects or stress raisers on Si are expected to be incorporated into the fully oxide layer and eliminated largely during the thermal oxidation and simultaneous annealing process. The thickness of the thermal oxide can be well established by controlling the annealing temperature and oxidation time. Figure 2c shows the ADF-STEM image (left) as well as the high-resolution SE image (right) of the same thermally-oxidized Si particle, which was annealed in dry air at ≈800 °C for 30 min. We can see that Si particles after the thermal oxidation inside the furnace get much smoother. To detect the compositions of the oxide before and after annealing, X-ray photoelectron spectroscopy (XPS) analyses were performed on the as-grown and thermally-oxidized Si particles. XPS is a surface-sensitive quantitative spectroscopic technique to identify the elemental composition and the chemical state of the material surface. As shown in Figure 2d, 2p Si XPS spectra of the particles after thermal oxidation exhibit obviously enhanced peak intensity at ≈103.5 eV, which is indicative of SiO_2 formation.[21] By contrast, the as-grown Si particles show a small and broad peak at ≈102.8 eV, indicative of the formation of the silicon sub-dioxide (SiO_x, $0<x<2$),[22] i.e., the SiO_x native layer turns into stoichiometric SiO_2 and the regrown surface oxide is also SiO_2 during the thermal oxidation. The inset high-resolution TEM images in Figure 2d demonstrate that both the native and thermally-grown oxide layers are amorphous. The passivated thermal oxide whose growth rate and properties depend weakly on Si crystal orientation[23] has an average thickness of ≈7 nm (see the thickness distribution in the inset histogram in Figure S3, Supporting Information). Note that if we increase the annealing temperature or oxidation time, the oxide will become thickened, and hence the volumetric fraction of the oxide layer in a particle tends to be more and more significant. Therefore, on one hand, we should make sure that the surface oxide is well passivated to incorporate the surface stress raisers and defects into

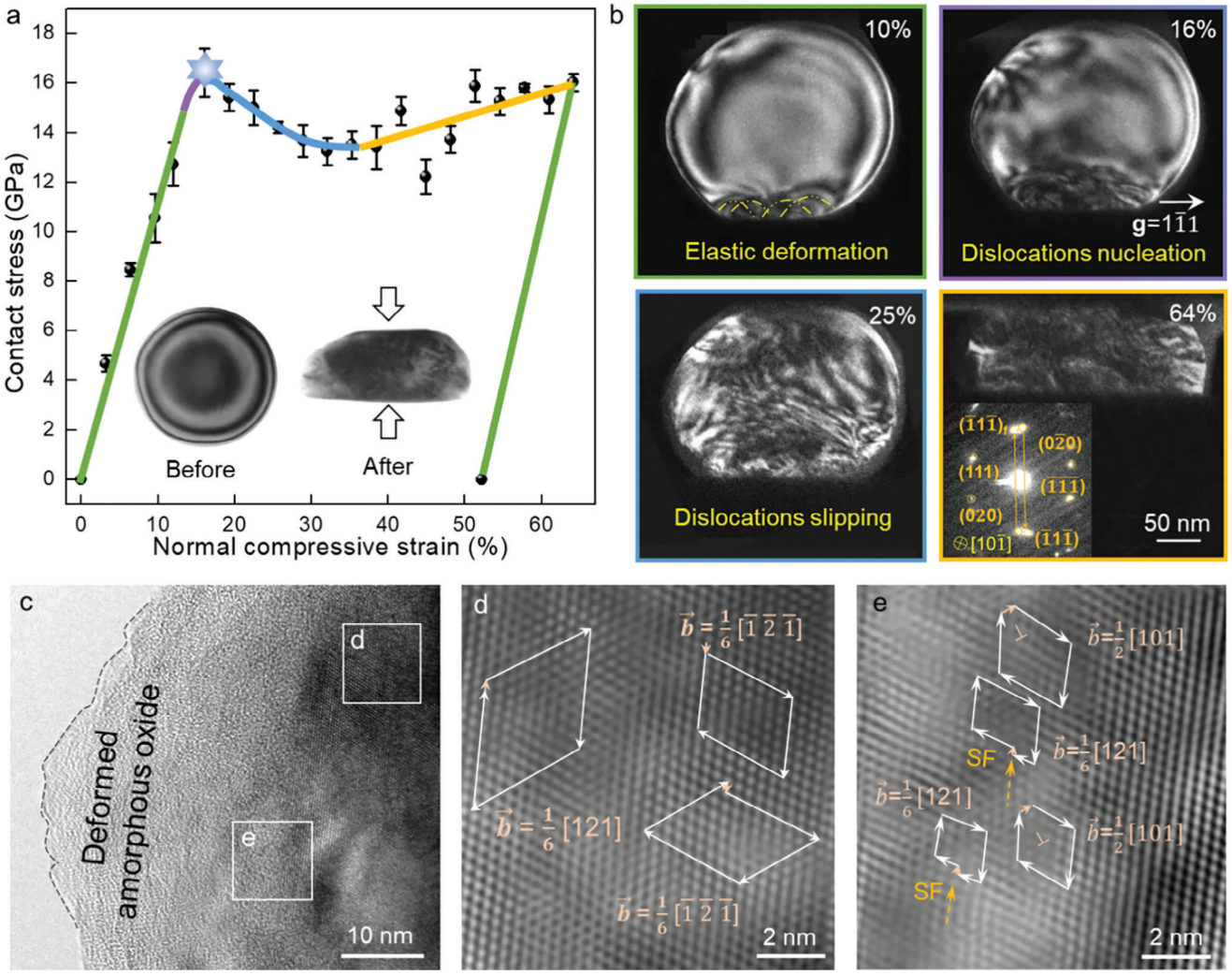

Figure 3. In situ compression of the individual thermally-oxidized Si particle. a) The contact stress versus compressive strain curve of a thermally-oxidized Si particle with the diameter of 265 nm. The insets show the TEM images of the particle before and after compression. Typical deformation regimes are marked in different colors. b) Series of the centered dark-field TEM images obtained using the (1$\bar{1}$1) reflection from the particle view along [101] zone axis demonstrates the deformation process at different compressive strains. The inset shows the selected area diffraction pattern of the compressed particle. c) The postmortem HRTEM characterizations of the thermally-oxidized Si particle. d) The filtered HRTEM image of a less distorted region with the Burgers circuits around dislocations. e) The filtered HRTEM image of the region is very close to the amorphous oxide surface and severely deformed.

it; on the other hand, the most part of the particles should remain to be single-crystalline Si. The effect of the oxide volumetric fraction on the mechanical behaviors of Si particles will be discussed further later.

2.3. In Situ Compression of the Thermally-Oxidized Si Particles

To check the surface healing effect on the strength and deformability of Si particles, thermally-oxidized ones were individually compressed inside TEM, and **Figure 3** displays the in situ compressive process of a representative particle (with D = 265 nm, and the thermal oxide layer of ≈8.5 nm). For comparison with the as-grown particle shown in Figure 1, this Si particle was also compressed along the ≈<111> direction. The corresponding contact stress (true stress) versus normal compressive strain curve is presented in Figure 3a. Here the contact stress is defined as the force sustained by the Si sphere divided by the contact area ($\pi D_i^2/4$, where D_i is the instantaneous contact diameter and can be directly measured from the recorded video). TEM images of the thermally-oxidized Si particle before and after compression were inserted in Figure 3a. Four deformation regimes (marked by different colors in the stress–strain curve) have been observed during compression. A correlation of each regime of the stress–strain curve with the real-time DF-TEM images (obtained using the (1$\bar{1}$1) reflection) captured from the Video S2 (Supporting Information) is demonstrated in Figure 3b. First, the thermally-oxidized particle experiences linear elastic deformation upon loading up to ≈10% with the corresponding stress of ≈15 GPa (as indicated by the green line). Upon the initial

contact, strain fringes emanate from the contact area, owing to the synergic elastic deformation of the thermally-grown oxide layer with the inner Si crystal. The uniform and symmetry distribution of multiple strain fringes predicts a relatively homogeneous distribution of the dislocation nucleation sites, as marked by the yellow contours in Figure 3b (≈12% strain). As the stress increases, the deformation enters the second regime, characterized by the stress–strain curve slightly deviating from the linear-elastic response (marked in purple), corresponding to the dislocation initiation. During the 12–16% strain range, dislocations nucleate and multiply rapidly near the contact area, contributing to incipient plastic deformation. When it reaches the upper yield point (defined as the yield strength of the thermally-oxidized particle) at ≈16.4 GPa, the deformation comes into the next regime (marked in blue), during which the contact stress decreases and ends at a lower yield point (≈35%, ≈13.5 GPa). In this regime, dislocations extend gradually across the particle, as observed by the development of some parallel contrast bands along {111} slip planes (see the captured TEM image at ≈25% compressive strain). The stress drop is assumed to be associated with the gradual initiation of small surface steps during the dislocation emergence and slip. Upon further compression with a fully flat contact between the deformed particle and the punch, the deformation enters the strain hardening regime (marked in orange). High-density dislocations multiply and interact with each other or with the oxide/Si interface (back stress), resulting in the stress increase as the strain continues (strain hardening). The smooth and continuous compression over 60% shows no sign of cracking or deformation localization, and the spherical particle was homogeneously shaped into a "pancake". It should be noted that e-beam irradiation is not dominant for the enhanced plastic deformability of the thermally-oxidized Si particles, which remain plastically deformable under compression without the e-beam illumination (see Figure S4, Supporting Information). No detectable amorphization or other phase transformation occurs in the deformed particle, as verified by the selected area electron diffraction pattern, which only shows an obvious splitting feature due to the appearance of abundant dislocations and stacking faults (see Figure 3b inset).

Figure 3c displays the postmortem high-resolution TEM (HRTEM) image obtained from the near-surface regions of the compressed Si particle. Clearly, we can see that the thermally-grown amorphous oxide surface deforms together with the interior crystal, without cracking or shear offset. To identify the deformation defects inside the particle, we used the Fourier Transform to filter the original HRTEM image to eliminate the aperiodic oxide information. High-density ($\approx 10^{16}$ m^{-2}) dislocations and stacking faults (SFs) can be observed from the enlarged and filtered images in Figure 3d,e; Figure S5, Supporting Information). By employing the Burgers circuit around the dislocation cores, their Burgers vectors, $\boldsymbol{b}$, can be determined. In a less distorted region, Shockley partial dislocations, with $\boldsymbol{b} = a/6[121]$ on {111} close-packed planes, have been identified (Figure 3d). In a severely deformed zone very close to the oxide surface (Figure 3e), besides the partial dislocations with stacking faults, the Lomer lock dislocations with $\boldsymbol{b} = a/2[101]$ are formed via the interaction of two full dislocations $a/2[110] + a/2[0\bar{1}1]$ at the intersection of the two slip systems $a/2[110](111)$ and $a/2[0\bar{1}1](1\bar{1}1)$. The Lomer lock dislocation is a type of sessile dislocation that can act as a pinning point and impede the slipping of mobile dislocations.[24] The introduction of Lomer lock dislocations in the severely deformed region may explain the strain hardening arising at the late compression stage: dislocations interlock with each other on three equivalent {111} planes inclined at ≈19.5° to the <111> loading axis. For [111] compression in Si, the Schmid factor for partial dislocations on $(1\bar{1}1)[121]$ slip system is 0.35, while the maximum Schmid factor for full dislocations on {111}<110> slip system is 0.27. This means that the resolved shear stress for the former is higher. What's more, atomic simulations show that the Peierls' stress for full dislocation motion in Si is 3.8–4.5 GPa,[25] higher than that for partial dislocations, ≈3.3 GPa.[26] Therefore, the nucleation and motion of partial dislocations should be favored upon yielding. As stress increases, full dislocations which are more mobile than partials[27] are activated, and their slip accommodates the majority of strain until the formation of Lomer locks trap other dislocations and cause the strain hardening.

2.4. Near-Theoretical Strength of the Thermal-Oxidized Si Particles

The 16.4 GPa maximum contact stress (corresponding to the maximum resolved shear stress of 5.74 GPa in the slip system {111}<121> of the thermally-oxidized Si particle is approaching the ideal strength of <111>-oriented Si ($E_{<111>}/10$ = 19 GPa, $G_{\{111\}}/10$ = 6.69 GPa),[28] and is more than twice the compressive strength measured in the as-grown Si particle (7.8 GPa, Figure 1). In order to check if the thermally-oxidized Si particles compressed along other orientations display the near-theoretical strength and the obviously enhanced plasticity as well, we have measured and calculated the resolved shear stress (RSS)[13a] of each tested particles with and without thermal oxidation treatment. The RSS versus the applied normal compressive strain from 26 individual Si particles (diameters ranging from 150 to 600 nm) compression experiments is plotted in **Figure 4** (Figures S6 and S7, Supporting Information demonstrate the deformation morphologies of some representative Si particles compressed along different orientations). The data appear quite scattered, and the possible factors acting to scatter the RSS are listed as follows. First, the deformation behavior and strength of Si depend on the volumetric fraction of the oxide layer, v_O (see the yield strength as a function of v_O shown in Figure S8, Supporting Information). If $v_O < \approx 10\%$ (the as-grown Si particles), the oxide barrier is not thick or tight enough to suppress the surface dislocations nucleation and the subsequent brittle fracture; the thermally-oxidized Si particles with higher v_O (e.g., $v_O > \approx 40\%$) demonstrate excellent plastic deformability, but their strength is greatly compromised. This softening mainly results from the increasing proportion of silica (Young's modulus of SiO_2 is 70 GPa,[29] less than half of that in also see Figure S9, Supporting Information). The RSS of the thermally-oxidized particles with $v_O \approx 20\%$ can approach the theoretical strength (Figure 4). Second, it has been well-established that the strength of single-crystalline Si has a relatively large orientation dependence. Therefore, the RSS variation with the loading direction is as expected. Third, some defects undetectable inside TEM may affect the strength of the tested samples, especially the thermally-oxidized Si particles with high plastic deformability, of which the yield strength is intimately

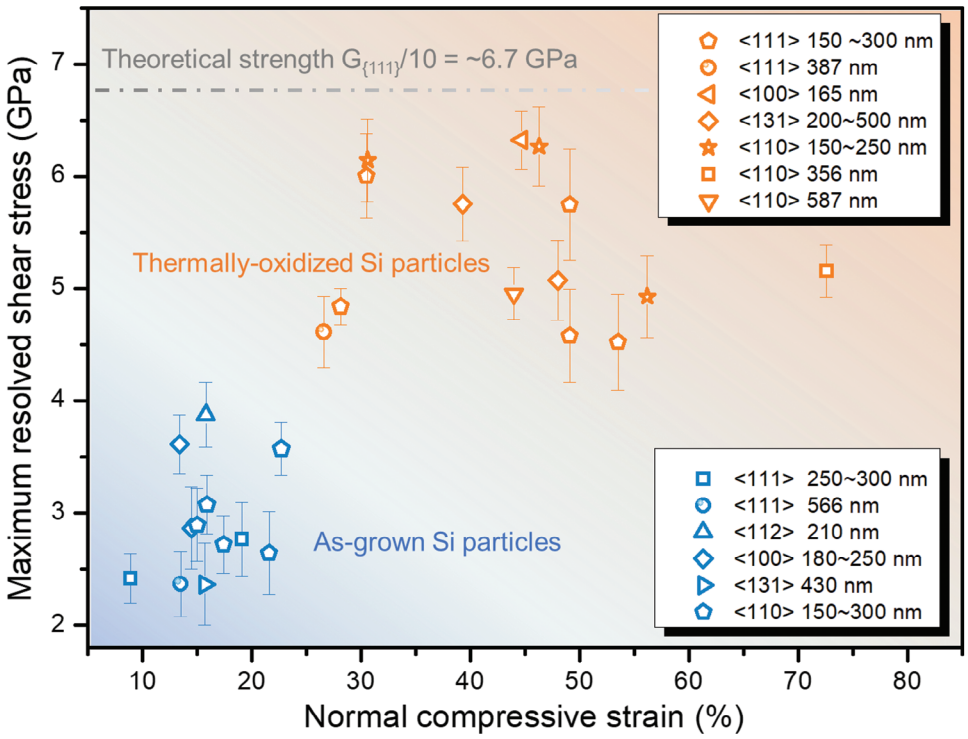

Figure 4. The maximum resolved shear stress versus the normal compressive strain in the as-grown (blue) and thermally-oxidized (orange) Si particles. The dashed horizontal lines in grey demonstrate the upper limit of the theoretical strength ($G_{\{111\}}/10 = 6.69$ GPa, where $G\{111\}$ is the shear modulus of {111} crystal planes). The size of these particles is ranged from 150 to 600 nm.

related with the defects evolution. Despite the scatter, the thermally-oxidized particles are still much more robust than their as-grown counterparts, and many of them obtain the strength approaching the theoretical value (≈6.7 GPa, as marked by the horizontal dashed lines in Figure 4).

2.5. Dislocation Mechanism Under the Combination of Ultrahigh Strength and Plasticity

As we have conceived in the introduction section, the smoother and passivated thermal oxide not only incorporates the initial surface pits or other possible defects into itself but also softens the contacts of Si particles with the substrate and punch, eliminating the possibility of the surface dislocation nucleation. However, besides the surface, the crystalline Si/amorphous oxide interface with some native point defects or other imperfections[12b,30] is also one of the preferred sites for the dislocation initiation. In the as-grown Si particles, prior to the incipient fracture, the very first plastic event may take its origin from these defects at quite low stresses. After the thermal oxidation treatment coinciding with the high-temperature annealing, the atomic defects (such as oxygen vacancies and Si interstitials) at the well-annealed Si/oxide interface could be annihilated via the oxide regrowth and the recombination of interstitials with vacancies.[20] As such, the thermally-grown oxide from SiO_x ($0<x<2$) to SiO_2 is accompanied with defect reduction at the interface, providing chances for the homogeneous dislocation nucleation in the interior crystal under much higher applied stress.

To further elucidate the influence of regrown amorphous surface layers on dislocations, molecular dynamic (MD) simulations were performed. For the as-grown Si particle ($D = 24$ nm), some sub-nanometer pits on the 1 nm amorphous layer were generated randomly to simulate its native surface; the thermally-oxidized Si particle ($D = 24$ nm) is modeled as the pristine Si crystal coated with a continuous and smooth amorphous layer (2 nm). For simplicity, the modeled two particles are also denoted as the as-grown and thermally-oxidized. **Figure 5** demonstrates the von Mises stress distribution and dislocations evolution in two particles at different compressive strains. The strain and the compressive stress corresponding to the onset of dislocation nucleation is 6% (7.5 GPa) and 21% (21.4 GPa), respectively, in the as-grown and thermally-oxidized particles. The enlarged views of the first dislocations demonstrate their nucleation sites (Figure 5a,e, right upper panel) as well as the local stress distribution in z-direction around the dislocations (Figure 5a,e, right lower panel). We can see that in the as-grown particle, the partial dislocation ($\boldsymbol{b} = 1/6<112>$, pink lines) initiates at the amorphous/crystalline interface due to the local stress concentration caused by pits, and then with increasing strains, full dislocations ($\boldsymbol{b} = 1/2<110>$, black lines) are activated in the interior (Figure 5b). Whereas in the thermally-oxidized particle, the full dislocation together with the partial dislocation is generated inside the crystalline Si (Figure 5e). Though both partial and full dislocations are activated in two particles, the partial dislocation slipping is more favored in the as-grown one, and full dislocations are dominant in the thermally-oxidized one (see Figure S10, Supporting Information). As strain increases, the significant

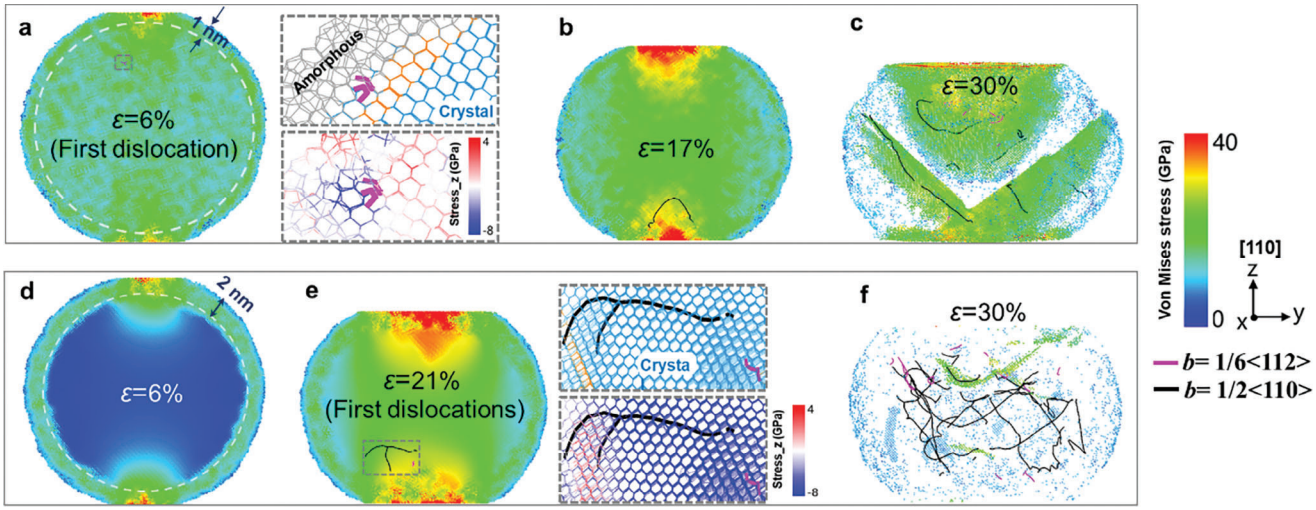

Figure 5. MD simulations on von Mises stress distributions and dislocations evolution in the 24 nm Si particles with different surface conditions. a) The cross-section of the Si particle with 1 nm rough amorphous layer at compressive strain $\varepsilon = 6\%$, corresponding to the generation of the first dislocation, i.e., the yielding point or the onset of plastic deformation. The enlarged view of the framed region shows the dislocation generation site (upper panel) and the local stress distribution in *z*-direction around the dislocation (lower panel); b) $\varepsilon = 17\%$; c) $\varepsilon = 30\%$. d) The cross-section of the Si particle with 2 nm smooth amorphous layer at compressive strain $\varepsilon = 6\%$; e) $\varepsilon = 21\%$, corresponding to the generation of the first dislocations. The enlarged view of the framed region showing the dislocation generation sites (upper panel) and the local stress distribution in *z*-direction around the dislocations (lower panel); f) $\varepsilon = 30\%$. In (c) and (f), for more clear demonstration of dislocations inside deformed particles, atoms with shear strains <0.6 are removed (except for those showing the contourlines). The partial dislocations with the Burgers vector $\boldsymbol{b} = 1/6\langle 112\rangle$ and the full dislocations with the Burgers vector $\boldsymbol{b} = 1/2\langle 110\rangle$ inside the two particles are demonstrated in pink and black lines, respectively.

dislocation activities in two intersecting {111} planes of the as-grown Si particle cause the localized deformation followed by the large shear-off (Figure 5c). In the thermally-oxidized particle, dislocations, especially the more mobile full dislocations,[27] nucleate homogeneously at high stress (near-theoretical strength) and slip in the interior. The high-density dislocations are confined by the continuous amorphous barrier and cannot escape out the surface (Figure 5f), inhibiting the obvious shear-off induced deformation localization and making the homogeneous deformation into a "pancake" possible. The dislocation back stresses from the amorphous barrier would ameliorate the local stress near the potential crack nucleation sites in the Si interior. Besides, the compressive stress from the confinement effect of the soft and smooth amorphous barrier (see Figure S11, Supporting Information) can effectively inhibit the crack initiation at the surface.

Since the classic paper of Atalla et al.,[31] the passivation of the silicon surface via thermal oxidation has become the dominant way for surface stabilization and surface or interface defect reduction in device technology.[32] As for small Si particles with the prevailing role of surfaces, thermal oxidation can not only improve the mechanical stability but also modify or functionalize the surface: the surface oxide transformation from SiO_x to SiO_2 allows to tune of the surface properties of Si particles for new features in, e.g., energy harvesting and storage, light emitting devices,[18a] imagery and drug/gene delivery in biomedicine[33] or catalysis,[34] etc. Taking one of the most important applications of Si particles as the anode material in high-energy lithium-ion batteries for example. The stress or strain caused by crumbling or even pulverization of Si during the lithiation reaction is a very big concern. The conformal oxide coating of Si anode particles is an effective strategy to reduce the excessive solid–electrolyte interface formation as well as suppress the volume expansion-induced cracking for improving the mechanical integrity.[35] We performed the in situ electrochemical lithiation on individual as-grown and thermally-oxidized Si particles inside TEM: a crack initiates at the former surface with the ≈45% volumetric expansion upon lithiation, while no cracks have been observed on the latter even when the volume strain reaches up to ≈345%, which is close to the theoretical limit at full lithiation (see Figure S12, Supporting Information for more details and explanations).

To recapitulate, three effects from the thermal oxidation mediated surface healing may have come into play for realizing the near-theoretical strength and ultrahigh plasticity in the robust Si particles: i) the incorporation of surface stress raisers or defects into the regrown oxide coating; ii) the annihilation of defects in the stoichiometric SiO_2 oxide or at the Si/oxide interface during the thermal annealing. Therefore, the near-surface regions that are usually perceived as the preferred initiation sites of brittle cracking become "blunt and ductile"; iii) the introduction of the compressive stress at the thermally oxidized surface. The surface compressive stress or the confining pressure can inhibit strain localization and crack initiation during severe deformation or volumetric expansion.

3. Conclusion

In summary, by virtue of the well-controllable thermal–oxidation–mediated surface healing effect, we have united the ultrahigh plasticity with the near-theoretical yield strength in submicron-sized Si particles, and in contrast to the as-grown counterparts that show initial elastic loading followed by catastrophic failure at a much lower stress. The real-time TEM

observations and MD simulations shed light on the underlying mechanism. The thermal oxidation coating with a suitable thickness can not only improve the load-bearing-reliability of small-scale Si but also provide more chances for itself as a high-performance functional materials, for example as the high-capacity electrode materials for lithium-ion batteries. The thermal-oxidation-mediated surface healing has been proven to be an effective and feasible way to tune the mechanical, electrochemical performances of Si nanostructures by modifying or functionalizing their surfaces, and maybe it holds for other materials, that suffer from premature brittle failure during their services. The simplicity and environmental friendliness of this single-step process should make it well-accepted in both industrial and research environments. Our work is expected to provide new insights to tune the comprehensive properties of small-scale materials via surface engineering.

4. Experimental Section

Thermal Oxidation of Si Particles: Silicon particles of 50–800 nm in diameter were synthesized using a thermal plasma deposition technique by the China Jiangsu Jinlei Technology Co. Ltd. As-grown Si powders were dispersed on a quartz crucible and exposed in air completely. The quartz crucible was placed in a box furnace and then annealed at elevated temperatures. The temperature was increased from room temperature to ≈800 °C and maintained for 30 min, after which the furnace was turned off and Si powders were naturally cooled down to room temperature. X-ray photoelectron spectroscopy (XPS) analyses were performed with a Thermo Scientific spectrometer using a monochromatic Al K_α radiation of energy beam (1486.6 eV).

In situ Compression Test on Individual Si Particles: Si particles with diameters ranging from 150–600 nm were selected for in situ compression tests, and they were first individually dispersed on a specially designed wedge-shaped silicon substrate, which allows unobstructed TEM imaging during the compression. In situ compression tests were performed inside a JEOL-2100F TEM (200 kV) using a Bruker's Hysitron PI95 PicoIndenter with a flat diamond punch. The particle was compressed between the diamond punch and the substrate, and the deformation process was monitored in real-time (recorded at 10 frames per second by the Gatan 833 CCD camera). Given the spherical geometry of the Si nanoparticles, the orientation parallel with the loading direction is random when they are deposited onto the substrate. Therefore, more than one hundred of nanoparticles and chose those aligned along the common orientations, such as <111>, <110>, <100> etc., for in situ compression experiments were characterized. The quantitative compression was run in the displacement-control mode with the constant loading/unloading rates of 2 nm s^{-1}. The displacement of the punch as well as the contact diameter of the particle with the punch were directly measured from the recorded video. A circular contact area is assumed to calculate the contact stress and the normal compressive strain. Normal compressive strain (defined as the compression displacement of the particle *z*, divided by its diameter, *D*).

MD (Molecular Dynamics) Simulation: MD simulations are performed using the Large Scale Atomic/Molecular Massively Parallel Simulator (LAMMPS).[36] The time step was 2 fs and the temperature was controlled using a Nose-Hoover thermostat.[37] Spherical samples of size 24 nm in diameter (361759 atoms) are used. One configuration is a 10 nm radius Si crystal with a 2 nm thick amorphous Si layer wrapped around the outside; the other configuration is a 11 nm radius Si crystal with a 1 nm thick amorphous Si layer wrapped around the outside and some atoms were deleted from the amorphous Si layer to make random 0–1 nm holes. Uniaxial compression is achieved by using a moving virtual planar indenter. Infinite hard indenters were set up using a force field parameter equal to 1000 eV $Å^{-3}$.[38] The planar indentation was placed above the sphere and moved down along the [1 1 0] direction at a constant speed of 0.1 Å ps^{-1} during compression. This corresponds to engineering strain rates of 4×10^8 s^{-1} for 24 nm diameter sphere, which is typical of molecular dynamics simulations. The silicon nanoparticles were relaxed for 2 ns to obtain an equilibrium state before applying the load. The MEAM potential by Baskes[39] was used which is considered to be the most reliable potential for predicting brittle fracture of silicon.[40] The atomic structures were visualized with the Open Visualization Tool (OVITO) software package.[41]

Statistical Analysis: A quantitative compression test on tens of individual Si nanoparticles was performed. For each particle, its contact stress with the diamond punch is defined as the applied force divided by the contact area ($\pi D_i^2/4$, where D_i is the instantaneous contact diameter and can be directly measured from the recorded video). To minimize errors of the calculated stress value, each D_i was measured for three times, and the error bars indicate statistical errors in terms of the standard deviations.

Supporting Information

Supporting Information is available from the Wiley Online Library or from the author.

Acknowledgements

The authors acknowledge the support from the National Natural Science Foundation of China (no. 52272162) and the National Key R&D Program of China (no. 2022YFB3203600). Y.W. gratefully acknowledges the support of K.C. Wong Education Foundation. Y. W. and W.X. thank Chuanwei Fan in Xi'an Jiaotong University for the technical support in mechanical data analysis.

Conflict of Interest

The authors declare no conflict of interest.

Author Contributions

W.X. and J.Y. contributed equally to this work. Y.W. conceived the project and supervised it with Z.S. W.X. carried out the experimental investigations with assistance from, Y.G., L.D., L.Z., X.W., and S.Z.; J.Y. and J.D. conducted the MD simulations; The data presentation was designed by Y.W. and W.X., with the assistance from J.Y. and J.D. The writing of the paper was led by Y.W. and W.X. All the authors contributed to the discussions.

Data Availability Statement

The data that support the findings of this study are available in the supplementary material of this article.

Keywords

in situ TEM compression, Si particles, surface healing, thermal oxidation

Received: March 18, 2024
Revised: May 9, 2024
Published online: May 20, 2024

[1] a) W. Liu, Y. Liu, Z. Yang, C. Xu, X. Li, S. Huang, J. Shi, J. Du, A. Han, Y. Yang, G. Xu, J. Yu, J. Ling, J. Peng, L. Yu, B. Ding, Y. Gao, K. Jiang, Z. Li, Y. Yang, Z. Li, S. Lan, H. Fu, B. Fan, Y. Fu, W. He, F. Li, X. Song, Y. Zhou, Q. Shi, *Nature* **2023**, *617*, 717; b) B. Wang, Z. Zhang, K. Chang, J. Cui, A. Rosenkranz, J. Yu, C. T. Lin, G. Chen, K. Zang, J. Luo, N. Jiang, D. Guo, *Nano Lett.* **2018**, *18*, 4611.

[2] T. Yi, L. Li, C. J. Kim, *Sens. Actuators, A* **2000**, *83*, 172.
[3] a) T. Tsuchiya, *J. Micromech. Microeng.* **2021**, *32*, 013003; b) Z. Zhang, X. Wang, F. Meng, D. Liu, S. Huang, J. Cui, J. Wang, W. Wen, *J. Manuf. Processes* **2022**, *75*, 617.
[4] J. R. Rice, R. Thomson, *Philos. Mag. (1798-1977)* **2006**, *29*, 73.
[5] a) J. Amodeo, K. Lizoul, *Mater. Des.* **2017**, *135*, 223; b) S. Chen, F. Liu, B. Liu, X. Chen, X. Ke, M. Zhang, X. Tang, P. Guan, Z. Zhang, Z. Shan, Q. Yu, *Mater. Today* **2022**, *55*, 37; c) Q. Liu, L. Wang, S. Shen, *Comput. Mater. Sci.* **2015**, *101*, 267; d) V. A. Eremeyev, *Acta Mech.* **2015**, *227*, 29.
[6] X. Cui, Z. Zhang, S. Yu, X. Chen, C. Shi, H. Zhou, F. Meng, J. Yu, W. Wen, *Nanoscale* **2023**, *15*, 9304.
[7] a) K. Y. Yasumura, T. D. Stowe, E. M. Chow, T. Pfafman, T. W. Kenny, B. C. Stipe, D. Rugar, *J. Microelectromech. Syst.* **2000**, *9*, 117; b) D. J. Young, C. A. Zorman, M. Mehregany, *Springer Handbook of Nanotechnology* (Ed: B. Bhushan), Springer Berlin Heidelberg, Berlin, Heidelberg **2004**, p. 225.
[8] M. Chen, L. Petho, A. S. Sologubenko, H. Ma, J. Michler, R. Spolenak, J. M. Wheeler, *Nat. Commun.* **2020**, *11*, 2681.
[9] H. Zhang, J. Tersoff, S. Xu, H. Chen, Q. Zhang, K. Zhang, Y. Yang, C. S. Lee, K. N. Tu, J. Li, Y. Lu, *Sci. Adv.* **2016**, *2*, e1501382.
[10] A. R. Beaber, J. D. Nowak, O. Ugurlu, W. M. Mook, S. L. Girshick, R. Ballarini, W. W. Gerberich, *Philos. Mag.* **2011**, *91*, 1179.
[11] a) Y. C. Wang, W. Zhang, L. Y. Wang, Z. Zhuang, E. Ma, J. Li, Z. W. Shan, *NPG Asia Mater.* **2016**, *8*, e291; b) Y.-c. Wang, D.-g. Xie, X.-h. Ning, Z.-w. Shan, *Appl. Phys. Lett.* **2015**, *8*, 106.
[12] a) M. Chen, J. Wehrs, A. S. Sologubenko, J. Rabier, J. Michler, J. M. Wheeler, *Mater. Des.* **2020**, *189*, 108506; b) J. Guénolé, J. Godet, S. Brochard, *Phys. Rev. B* **2013**, *87*, 045201.
[13] a) W. Z. Han, L. Huang, S. Ogata, H. Kimizuka, Z. C. Yang, C. Weinberger, Q. J. Li, B. Y. Liu, X. X. Zhang, J. Li, E. Ma, Z. W. Shan, *Adv. Mater.* **2015**, *27*, 3385; b) R. Gu, A. H. W. Ngan, *Acta Mater.* **2012**, *60*, 6102.
[14] a) S. J. Grutzik, E. Milosevic, B. L. Boyce, A. T. Zehnder, *J. Appl. Phys.* **2015**, *118*, 195304; b) T. Alan, A. T. Zehnder, D. Sengupta, M. A. Hines, *Appl. Phys. Lett.* **2006**, *89*, 231905.
[15] J. A. El-Awady, S. I. Rao, C. Woodward, D. M. Dimiduk, M. D. Uchic, *Int J Plast* **2011**, *27*, 372.
[16] a) F. Östlund, K. Rzepiejewska-Malyska, K. Leifer, L. M. Hale, Y. Tang, R. Ballarini, W. W. Gerberich, J. Michler, *Adv. Funct. Mater.* **2009**, *19*, 2439; b) J. D. Nowak, A. R. Beaber, O. Ugurlu, S. L. Girshick, W. W. Gerberich, *Scr. Mater.* **2010**, *62*, 819.
[17] a) K. L. Johnson, *Contact Mechanics*, American Society of Mechanical Engineers, New York **1985**; b) T. Zhu, *J. Mech Phys. Solids* **2004**, *52*, 691.
[18] a) Z. Kang, Y. Liu, S. T. Lee, *Nanoscale* **2011**, *3*, 777; b) X. H. Liu, L. Zhong, S. Huang, S. X. Mao, T. Zhu, J. Y. Huang, *ACS Nano* **2012**, *6*, 1522.
[19] N. P. Rao, H. J. Lee, M. Kelkar, D. J. Hansen, J. V. R. Heberlein, P. H. McMurry, S. L. Girshick, *Nanostructured Materials* **1997**, *9*, 129.
[20] K. Taniguchi, Y. Shibata, C. Hamaguchi, *J. Appl. Phys.* **1989**, *65*, 2723.
[21] V. G. Kesler, S. G. Yanovskaya, G. A. Kachurin, A. F. Leier, L. M. Logvinsky, *Surf. Interface Anal.* **2002**, *33*, 914.
[22] R. Alfonsetti, L. Lozzi, M. Passacantando, P. Picozzi, S. Santucci, *Appl. Surf. Sci.* **1993**, *70*, 222.
[23] S. M. Sze, *Quantum Electronics IEEE Journal* **1981**, *15*, 1438.
[24] R. Madec, B. Devincre, L. P. Kubin, *Phys. Rev. Lett.* **2002**, *89*, 255508.
[25] L. Pizzagalli †, P. Beauchamp, *Philos. Mag. Lett.* **2004**, *84*, 729.
[26] J. Godet, J. Rabier, *J. Phys.: Conf. Ser.* **2019**, *1190*, 012007.
[27] L. Pizzagalli, P. Beauchamp, *Philos. Mag. Lett.* **2008**, *88*, 421.
[28] J. Kim, D.-i. Cho, R. S. Muller, Berlin, Heidelberg. **2001**, *662*, 665.
[29] S. Inaba, S. Fujino, K. Morinaga, *J. Am. Ceram. Soc.* **2004**, *82*, 3501.
[30] J. Godet, F. A. El Nabi, S. Brochard, L. Pizzagalli, *Phys Status Solidi A Appl Mater Sci* **2015**, *212*, 1643.
[31] M. M. Atalla, E. Tannenbaum, E. J. Scheibner, *Bell Syst. Tech. J.* **1959**, *38*, 749.
[32] W. Füssel, M. Schmidt, H. Angermann, G. Mende, H. Flietner, *Nucl. Instrum. Methods Phys. Res., Sect. A* **1996**, *377*, 177.
[33] R. Ghosh Chaudhuri, S. Paria, *Chem. Rev.* **2011**, *112*, 2373.
[34] S. Fernández, L. Gao, J. P. Hofmann, J. Carnis, S. Labat, G. A. Chahine, A. J. F. van Hoof, M. W. G. M. Verhoeven, T. U. Schülli, E. J. M. Hensen, O. Thomas, M. I. Richard, *Nanoscale* **2019**, *11*, 331.
[35] a) H. K. Song, K. T. Lee, M. G. Kim, L. F. Nazar, J. Cho, *Adv. Funct. Mater.* **2010**, *20*, 3818; b) J. Cho, T. J. Kim, Y. J. Kim, B. Park, *Electrochem. Solid-State Lett.* **2001**, *4*, A159.
[36] S. Plimpton, *J Comput Phys* **1995**, *117*, 1.
[37] W. G. Hoover, *Phys. Rev. A* **1985**, *31*, 1695.
[38] a) D. Kilymis, C. Gérard, J. Amodeo, U. V. Waghmare, L. Pizzagalli, *Acta Mater.* **2018**, *158*, 155; b) S. Bel Haj Salah, C. Gerard, L. Pizzagalli, *Comput. Mater. Sci.* **2017**, *129*, 273.
[39] M. I. Baskes, *Phys. Rev. B* **1992**, *46*, 2727.
[40] J. G. Swadener, M. I. Baskes, M. Nastasi, *Phys. Rev. Lett.* **2002**, *89*, 085503.
[41] A. Stukowski, *Modell. Simul. Mater. Sci. Eng.* **2010**, *18*, 015012.